Early stages of iron anodic oxidation: Defective growth and density increase of oxide layer

Hiromasa Fujii,[1,2,3,*] Yusuke Wakabayashi,[2,3,†] and Takashi Doi[4]

[1]*Division of Materials Physics, Graduate School of Engineering Science, Osaka University, Toyonaka 560-8531, Japan*
[2]*Department of Physics, Tohoku University, Sendai 980-8578, Japan*
[3]*Materials Research Center for Element Strategy, Tokyo Institute of Technology, Yokohama 226-8501, Japan*
[4]*Research and Development, Nippon Steel Corporation, Amagasaki, Hyogo 660-0891, Japan*

(Received 25 December 2019; accepted 18 February 2020; published 3 March 2020)

The early stages of anodic oxidation in the potentiostatic condition at the interface between a borate buffer solution at pH 8.4 and Fe(100), (110), and (111) surfaces are investigated by sub-second resolution real-time x-ray reflectometry. The growth process is composed of three stages. The electron density of the inner-oxide layer for Fe(111) after a potential step from −0.8 to +0.7 V versus Ag/AgCl in the steady-state growth, stage III (1.65 s $< t$, where t denotes the time after the potential step), is 1.52 electrons/Å^3, which is close to the density of magnetite. The growth rate is proportional to t^{-1}, which follows the direct logarithmic law or point-defect model. In an earlier stage of the oxide film growth, stage II (0.4 $< t \leqslant$ 1.65 s), the growth rate is proportional to $t^{-1.5}$, while the electron density maintains the same value as that in stage III. At the first stage that can be discriminated by our time resolution, stage I ($t \leqslant$ 0.4 s), the growth rate is the same as that for stage II, i.e., proportional to $t^{-1.5}$, while the electron density significantly decreases. The suggested structure is a highly defective spinel oxide, and defects are filled by the end of stage I; there is no signature of the growth of other phases, such as hydroxide, as the inner layer. This behavior indicates that the early stage of the oxide film growth is faster than the formation of a complete spinel layer at the iron-oxide interface. The deviation of the growth rate from the point-defect model in stages I and II is caused by the strong electric field at the iron-oxide interface.

DOI: 10.1103/PhysRevMaterials.4.033401

I. INTRODUCTION

Surface oxidation of a metal is a general phenomenon that is induced when a metal surface is exposed to oxygen. Some metals form dense and stable oxides, which separate metal surfaces from their environments and render them chemically inactive. Despite their protective nature, oxide growth continues even after the whole surface is covered with the oxide, and eventually the growth is ceased at a certain thickness. The oxide film growth is a result of oxygen migration caused by the diffusion and electric field within the oxide film. The growth process has been electrochemically investigated for decades [1–4], while its microscopic mechanism is still under debate [5]. The thermodynamics of the film formation was discussed along with treating the interfacial atomic monolayer as a different phase from the bulk [6,7]. The key feature is a potential profile around the interface since the potential gap at the metal/oxide film interface, $\phi_{m/f}$, controls the oxidation reaction, and the potential gradient in an oxide thin film governs the ion migration. Typical models accepted so far are the Mott-Cabrera model [8] and the point-defect model (PDM) [9–11]. The Mott-Cabrera model assumes that the electric field in the oxide is $\Delta V/L$, where L is the film thickness and ΔV is the potential difference between the metal and the surroundings. This model leads to an inverse-logarithmic law, $1/L = \alpha \ln(t) + \beta$, where t denotes the time and α and β are constants. PDM postulates the electric field in an oxide is constant and independent of the thickness, and leads to the direct logarithmic law $L = \alpha \ln(t) + \beta$. Iron is a typical material that forms a thin oxide layer at the surface. Although the asymptotic behavior to the steady state is well reproduced by both models, an x-ray reflectivity study of an iron polycrystal revealed that PDM better reproduces the wide time-range (∼10 s to 4 h) growth behavior [12].

The growth of an oxide on iron is rapid, and is mostly completed within 1–10 s [13–16]. The growth rate at the early stage deviates from the PDM prediction [13,14,17]. The growth mechanism at the early stages has been an open question due to the insufficiency of direct experimental information. Most studies have measured only the macroscopic kinetics because of the difficulty in observing the microscopic procedure of the film growth. An electrochemical and ellipsometric study [14] suggested oxyhydroxide formation in the early stage of film growth from a comparison of the consumed total electric charge and film thickness. However, the electrochemical current greatly exceeded the values expected from the film thickness obtained by ellipsometry. Since the observed discrepancy is caused by other unidentified reactions, such as iron or oxide dissolution [14], the combined interpretation of the current and thickness is ambiguous. It is preferable to investigate the kinetics and structure at the same time to understand the film growth mechanism at the early stage. The best technique for this purpose is the recently developed time-resolved x-ray reflectometry [17].

In the current study, the oxidation of iron (100), (110), and (111) surfaces in borate buffer solution at pH 8.4 under

*fujii@crystal.mp.es.osaka-u.ac.jp
†wakabayashi@tohoku.ac.jp

potentiostatic control is investigated by means of subsecond time-resolved synchrotron x-ray reflectivity measurements. Compared with our previous report [17], the experimental techniques are improved to determine the very early-stage electron density. The growth process is unambiguously clarified to comprise three distinct stages. In the early stages I and II, the growth rate is found to be approximately proportional to $t^{-1.5}$, while in stage III, the rate is proportional to t^{-1}, as explained by PDM. Furthermore, the electron density of the oxide layer in the initial stage of the film growth is 87% of that in the steady state, which strongly suggests a defective spinel oxide. Surface orientation does not affect the qualitative features of the kinetics, while the film growth rate in stage III depends on the surface orientation. This can be caused by the interfacial strain.

II. EXPERIMENT

Time-resolved x-ray reflectivity experiments with a monochromatic 25 keV x-ray beam were performed at the BL13XU of SPring-8, Japan. The beam size was selected as $300 \times 50\ \mu m^2$ for the grazing-incidence measurements. A two-dimensional pixel array detector PILATUS 100K (Dectris, Switzerland) was equipped to record the x-ray scattering signal. The stationary method [17] was employed for time-resolved measurements to realize a time resolution of 25 ms. The stationary method does not involve any mechanical movements of a diffractometer, while the ordinary scan method requires a mechanical scan involving sample rotation and detector movement; it takes at least tens of seconds to complete the reflectivity measurement. The camera length for the stationary method was 915 mm and for the ordinary scan method it was 740 mm. For time-resolved measurements, the detector was partially covered with lead and tantalum foil to measure the wide dynamic range scattering signal without the counting loss. The incident angle in the stationary measurement was selected as 0.1°, the critical angle of magnetite for the 25 keV x-ray beam, to enhance the signal from the surface. Only for the case of Fe(111) at +0.7 V were two data sets with incident angles of 0.1° and 0.8° collected, and they were connected at $q_z = 0.25$ Å^{-1} to achieve a better quality of the data.

Three Fe single crystals having flat (100), (110), and (111) surfaces with a sample area of 7 mm × 9 mm were prepared. To obtain the flat surfaces, the crystals were ground with alumina grit, then polished with colloidal silica slurry (COMPOL 80, Fujimi Inc., Japan). The roughness of the bare iron surface estimated by x-ray reflectivity results for the (100), (110), and (111) surfaces was 2.0, 2.2, and 2.6 Å, respectively. The sample was set in the electrochemical cell [18] with the shorter side perpendicular to the incident x rays, and immersed in borate buffer solution at pH 8.4. During the experiment, electrolyte was continuously deoxidized by bubbling N_2 gas and circulated to avoid possible effects by dissolved iron ions [19]. The electrical potential of the Fe, V, was controlled by an Ivium CompactStat potentiostat (Ivium Technologies B.V., the Netherlands) using a Ag/AgCl reference electrode. All potentials in this paper are relative to the Ag/AgCl electrode. The detector and the potentiostat were controlled remotely from one computer to synchronize the instruments. The response delay of the detector to the potentiostat was estimated by the initial change of the x-ray reflectivity, and the origin of the detector time was shifted by 75 ms for all data.

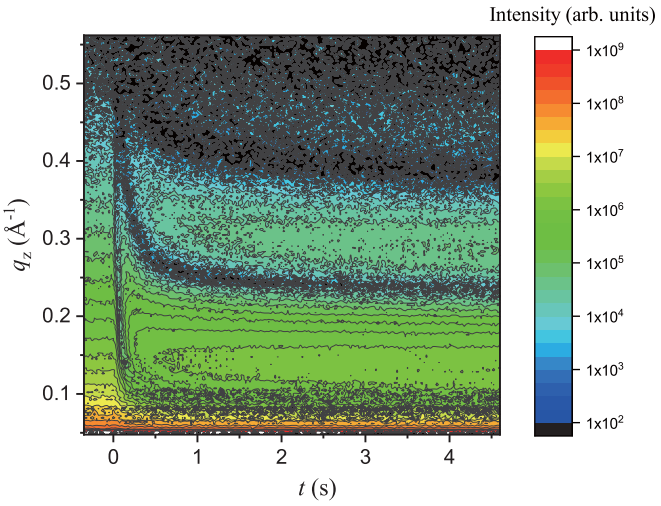

FIG. 1. Time evolution of x-ray reflectivity for Fe(111). The Fe potential was changed from −0.8 to +0.7 V at $t = 0$. The wide range of Q-space was measured with the time resolution of 25 ms.

Electrochemical current was monitored during reflectivity measurements to confirm that no unexpected reaction occurred. Prior to changing the potential, the surface oxide film was removed by cathodic reduction at −0.8 V for 20 min. The time evolution of the surface oxide film was investigated under potentiostatic control with a step from cathodic (−0.8 V) to anodic (+0.3, +0.5, and +0.7 V) potentials. Measurement time was 20 min for (111) and 30 min for (100) and (110) with the highest time resolution of 25 ms.

III. RESULTS AND ANALYSIS

The time evolution of the x-ray reflectivity profiles of the Fe (111) surface under a potential step from −0.8 to +0.7 V is depicted in Fig. 1. Profiles were collected by the stationary method and normalized by multiplying $I(-0.8\ \text{V}, q_z)/I_{\text{st}}(-0.8\ \text{V}, q_z)$, where $I_{\text{st}}(V, q_z)$ and $I(V, q_z)$ refer to the intensity at q_z at the potential V measured by the stationary and ordinary scan methods, respectively. The intensity at the total reflection condition was also measured in the scan method to scale the reflectivity intensity. Monotonous profiles along q_z for $t \leqslant 0$ represent the bare iron surface, while the oscillating features at $t > 0$ indicate the existence of a film whose thickness is indicated by the frequency of oscillations. Surface oxide rapidly formed within 1–2 s after switching the potential, which is consistent with our previous report [17]. Profile fittings were executed based on the Bayesian inference using the Monte Carlo sampling [20] to derive the most probable electron density profiles. Since this sampling method has an advantage in evaluating the uncertainty, it was suitable for our data with limited statistics due to the short exposure time. In our analysis, 10^6 samples were made, and recorded once in 10^2 to obtain 10^4 samples. The resultant parameter values and error bars at each t were calculated by the average and standard deviation of the last 2×10^3 recorded samples. For

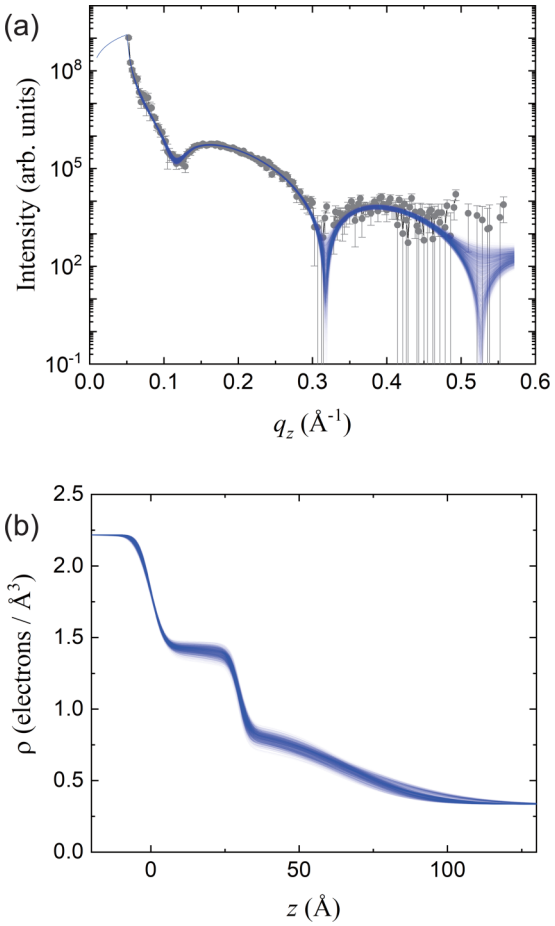

FIG. 2. (a) X-ray reflectivity and (b) electron density distribution for Fe(111) obtained 0.25 s after the potential step from −0.8 to +0.7 V. Closed symbols in (a) show experimental results, and the blue curves show the 2000 samples obtained by Monte Carlo sampling. Each curve is so thin that they appear to be a thick blurred curve. Corresponding electron densities are presented in (b). The plane at $z = 0$ corresponds to the Fe–inner-layer interface and that at $z \sim 30$ Å corresponds to the inner-layer–outer-layer interface. A large uncertainty is observed for the outer layer.

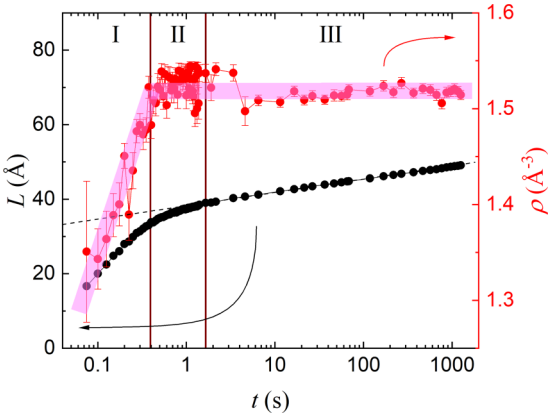

FIG. 3. Thickness L (black) and electron density ρ (red) of the inner-layer grown on Fe(111) at +0.7 V as a function of time t. Three distinct stages are observed. In stage I, the electron density is significantly lower than that in stages IIand III, and monotonically increases until the end of stage I. Direct logarithmic law $L = \alpha \ln(t) + \beta$ is followed only in stage III. The pink solid line is a guide for the eye. The error bars for L are smaller than the symbol size.

the analysis, a structural model was constructed as three slabs with seven parameters: electron density, the thickness and roughness of two slabs, which correspond to the inner and outer layers [4,17], and the roughness of the iron surface. The electron densities of the iron substrate and the borate buffer solution were fixed. Reflectivity from the slab model was calculated by the recursive Parratt formalism. A typical result of the analysis is presented in Fig. 2. The x-ray reflectivity profile for Fe(111) under +0.7 V at $t = 0.25$ s is displayed in Fig. 2(a) together with 2×10^3 simulated lines from sampling. Data points with small error bars were well reproduced by the calculated profiles, while those with large errors were poorly reproduced. The corresponding 2×10^3 electron density profiles are visualized in Fig. 2(b). The electron density for the outer layer had a larger uncertainty, and it showed a broader distribution than the inner layer.

The time evolution of the inner-layer thickness L and inner-layer electron density ρ during the −0.8 to +0.7 V potential step for Fe(111) is summarized in Fig. 3. We focused our attention on the two parameters because considerable changes were observed only in them. The observed growth process could be divided into three stages: stage I, in which the ρ is lower than the steady-state value ($t \leqslant 0.4$ s); stage II, in which the time evolution of L deviates from the PDM prediction, $\alpha \ln(t) + \beta$ ($0.4 < t \leqslant 1.65$ s); and stage III, the PDM region ($1.65 \text{ s} < t$). The electron density at stage Iwas lower than the density in later stages by up to 13%. It monotonically increased during stage Iand reached 1.52 electrons Å^{-3}, the same value as that achieved at the later stages. The time dependence of the inner-layer thickness showed the relation of $L = \alpha \ln(t) + \beta$ proposed by PDM in stage III, but deviated from the relation in stages Iand II.

The potential and surface-orientation dependences of the inner-layer growth are presented in Fig. 4. The growth processes at any potential and surface orientation qualitatively exhibited similar behaviors. The potential difference shown in Fig. 4(a) markedly effected the growth rate in stages Iand IIand only had a small effect in stage III. However, surface orientation influenced both the early and later stages [Fig. 4(b)]. A surface having a thicker film tended to show a higher growth rate in the later stage. The time evolution of the growth rate dL/dt is presented in Fig. 5. There was only a small voltage [Fig. 5(a)] and surface orientation [Fig. 5(b)] dependence, and a common trend was observed: $dL/dt \propto t^{-1.5}$ in stages Iand IIand $dL/dt \propto t^{-1}$ in stage III. Figure 6 presents dL/dt as a function of L under a series of potentials (a) and surface orientations (b). Apparent transitions were observed in all plots. The estimated electric field strengths inside the film under the PDM formalism based on the relationship [9] $E_0 = -k_B T/2e \times d/dL[\ln(dL/dt)]$ were $5.06(9) \times 10^5$, $3.74(7) \times 10^5$, and $3.30(4) \times 10^5$ V cm^{-1} for (100), (110), and (111), where k_B, T, and e are Boltzmann's constant, temperature (300 K in this case), and elementary charge, respectively. The obtained magnitude of the electric field was close to the typical value, 1 MV cm^{-1}.

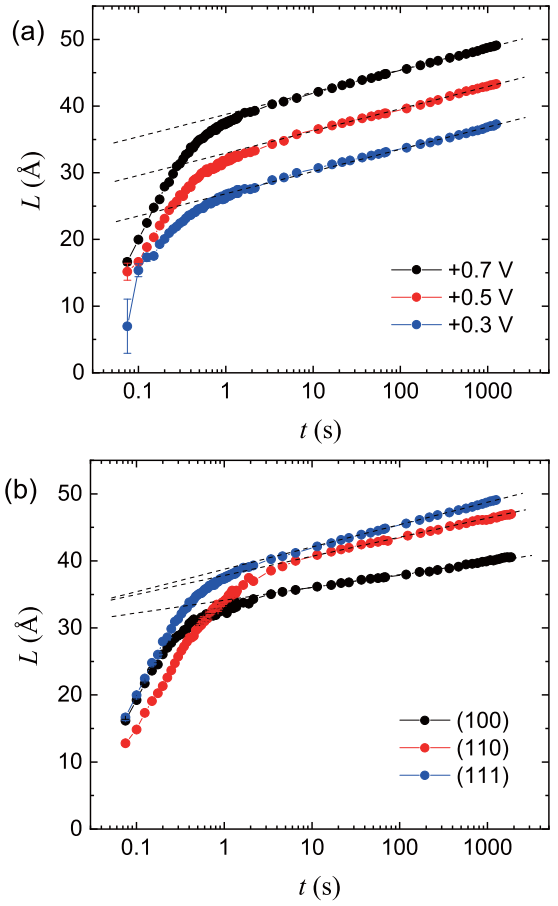

FIG. 4. Time evolution of the film thickness measured at (a) different potentials for Fe(111), and (b) different surface orientations at $V = +0.7$ V.

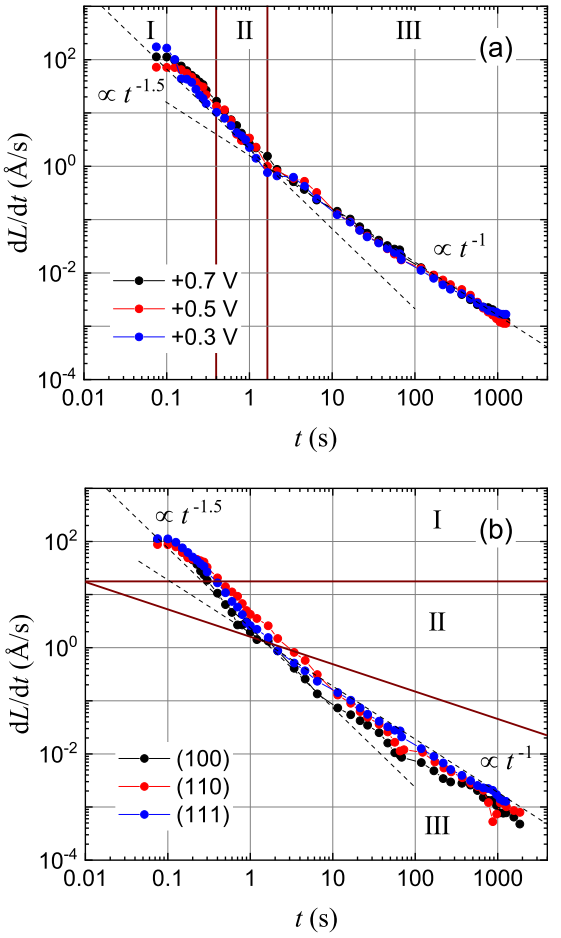

FIG. 5. Growth rate as a function of time for (a) Fe(111) at the potentials of +0.3, +0.5, and +0.7 V and for (b) Fe(100), (110), and (111) at +0.7 V. All data sets exhibit the same trend in which growth rates in the early stages follow $dL/dt \propto t^{-1.5}$ and in the later stage follow $dL/dt \propto t^{-1}$. The time evolutions following $t^{-1.5}$ and t^{-1} are shown by the dashed lines.

IV. DISCUSSION

The growth behavior in stage IIIis well explained by PDM following $dL/dt \propto \exp(-AL)$. Let us examine our experimental results with the aid of PDM. While the voltage in our experimental range had little effect on dL/dt in stage III, the surface orientation clearly influenced the growth rate. The steady-state thickness is known to depend on the voltage as $L = aV + b$, as derived from experiments [12,21,22] and also predicted by theory [10]. The observed values of the steady-state thickness in our experiments also showed good agreements with $L = aV + b$. Estimated parameters a for (100), (110), and (111) were 19.9, 27.8, and 29.5 Å V^{-1}, and those for b were 26.4, 27.2, and 28.5 Å, respectively. Here, the parameters were calculated from the linear fitting for datasets of +0.3, +0.5, and +0.7 V at $t = 20$ min. The effect of the Fe orientation on the oxide film growth can be ascribed to two factors: the electronic factor and the elastic factor. The former was estimated by the orientation dependence of the work function. The work function of iron changes by 0.15 eV with orientation, where the work function for (100) is 4.67 ± 0.03 eV [23] and that for (111) is 4.81 ± 0.02 eV [24]. The shift of the work function with a constant anode electric potential is equivalent to the shift of the anode electric potential with a constant work function. The higher work function corresponds to the higher electric potential, which makes the film thicker. Therefore, we expected a thicker film at steady state for (111) than (100) by $a \times 0.15$ V ~3.8 Å with $a = 25.7$ Å/V, the average value among a for the three orientations. Experimentally, the film on the (111) plane is thicker than that on the (100) plane by 7 Å, which agrees qualitatively with the above discussion. Quantitatively, however, the difference was too large to be ascribed to the work function, and some other effect is expected to explain the anisotropy of the film thickness. In addition, the orientation dependence of the work function could not reproduce the orientation-dependent growth rate in stage IIIsince the work function, or electric potential, does not affect the growth rate in stage IIIas shown in Figs. 4(a) and 5(a). Therefore, some elastic effects also play a role. It has been reported that the spinel films grown on Fe(100) and (110) surfaces are crystalline and the orientation is related to the substrate orientation [25]. The lattice mismatch for film(100)–Fe(100) is up to ~3% along the Fe[010] and [001] directions, and that for film(111)–Fe(110) is 27% along the Fe[$1\bar{1}0$] direction and 3% along the Fe[001] direction. Therefore, the films on Fe(100) feel

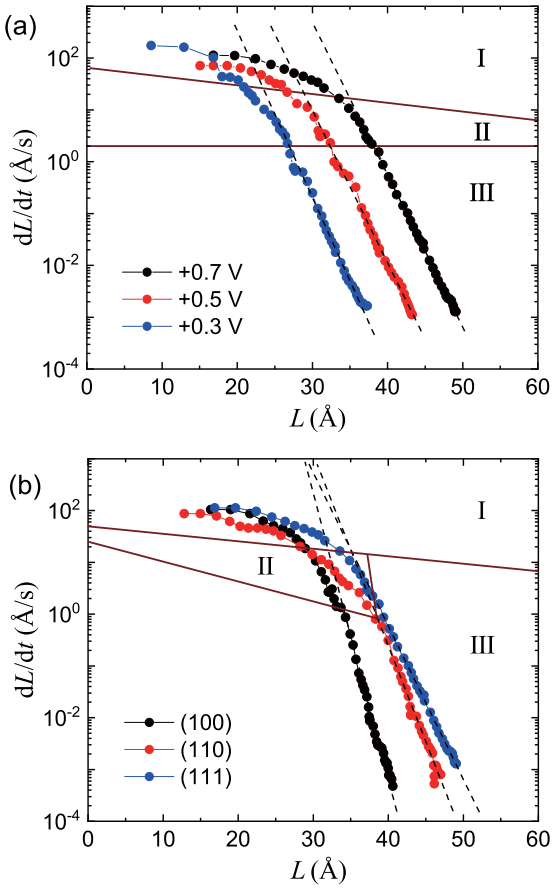

FIG. 6. Growth rate vs thickness for (a) Fe(111) under +0.3, +0.5, and +0.7 V, and for (b) Fe(100), (110), and (111) under +0.7 V. Three stages are observed for each set of data.

biaxial strain while those on Fe(110) feel only uniaxial strain because of the huge lattice mismatch along the Fe[1$\bar{1}$0] direction. Such a strain provides the growth-orientation-dependent Gibbs energy of oxide formation ΔG_d, where d denotes the Fe surface orientation. When we take ΔG_d into PDM, the growth rate is proportional to $\exp(-2\Delta G_d/\chi k_B T)$, where χ is the valence of the Fe ion. The difference in the film growth rate in stage IIIshown in Figs. 4(b) and 5(b) is reproduced by assuming the difference of the value of ΔG_d by less than room temperature. Based on the slow growth rate for the film on the (100) surface, a large $\Delta G_{(100)}$ is expected.

Stage IIshowed a different time evolution of the growth rate from the PDM formalism. Therefore, some assumptions in PDM are not justified at this stage, such as a constant electric field, which mainly controls the relationship between growth rate and thickness. The depth dependence of the electric field, which is modulated by the space charge layers at the interfaces, has been examined by numerically solving the transport and Poisson's equation in a film [26–28]. The typical thickness of the space charge layer derived in Refs. [26,28] was on the order of 1 nm, which coincides with the critical thickness between stage IIand stage III.

Stage Ifollows $dL/dt \propto t^{-1.5}$ and the thickness has less of an influence on the growth rate, as visualized in Fig. 6(a). Although the early stage, stage Iand/or IIin this case, has been regarded [13,14] as a diffusion-limited process following $dL/dt \propto t^{-1/2}$, the detailed x-ray reflectivity study apparently evidenced that diffusion does not dominate the growth rate. Additionally, the electron density of the film was reduced by up to 13%, as shown in Fig. 3. The minimum electron density observed with the present time resolution was 1.32(7) electrons Å^{-3}. The electron densities of possible oxides Fe_3O_4 [4,29–33], γ-Fe_2O_3 [30,31], and LAMM [25,34] are 1.53, 1.40, and 1.26 electrons Å^{-3}, respectively. Hydroxide and oxyhydroxide have lower electron densities such as 0.99, 0.95, 1.03, and 1.03 electrons Å^{-3} for α-FeOOH [35], γ-FeOOH [36], $Fe(OH)_2$ [37], and $Fe(OH)_3$ [38]. The observed electron density in stage Iwas comparable to spinel oxides but apparently higher than hydroxide and oxyhydroxide. Therefore, the film structure in the early stage should be a defective spinel oxide. The density monotonically increased with time in this stage. This meant that the vacancies were filled with migrated ions, and no other subphases are suggested. Compared with Fe_3O_4, the estimated chemical formula is $Fe_{2.3(2)}O_4$ or $Fe_3O_{1.1(2)}$ for the case in which the defect species was Fe^{3+} or O^{2-}. Since $Fe_3O_{1.1(2)}$ is chemically unstable, the defect species was likely to be iron ions or both iron and oxygen ions.

What is happening at the iron-spinel interface in stage IIis that Fe atoms at body-centered-cubic iron sites tend to move spinel sites nearby. At the interface, the electric potential changes abruptly by $\phi_{m/f} = B \times V - E_0 L + C$, where B and C are constants [9]. Therefore, the potential jump $\phi_{m/f}$ and the local electric field at the interface depend on L. In the PDM formalism, the ionic flow is treated to be proportional to the concentration gradient and to the electric field, i.e., a continuum model is employed. Here, we use an atomistic interpretation for PDM [12], which is similar to the Mott-Cabrera model [8,39]. In the atomistic interpretation, the potential profile has minima at each atomic site. A schematic of the potential profile of iron ions around the iron-oxide interface is presented in Fig. 7. The profiles for the continuum model are depicted by the thin curves, and those for the atomistic model are depicted by the thick curves. The continuum model gives a good picture for the small $\phi_{m/f}$ case in which the iron atoms are well trapped at the potential minima, and the activation energy for the iron hopping from the metal side to the oxide side is larger than the thermal fluctuation. The red potential profiles show a large $\phi_{m/f}$ case. In this case, the activation energy is smaller than the thermal fluctuation, and thus the iron atom at the metal side of the interface moves quickly to the oxide side of the interface. The transition is too fast to form a defect-free spinel structure, resulting in a thick spinel film with a lot of vacancies. The vacancies are filled with ions later. The increased cation flow across the metal/oxide interface reached the growth rate limited by another process, and the rate-limiting process is changed between stage Iand II. This is the reason why the growth rate shows no thickness dependence in stage I.

V. CONCLUSION

The time evolution of Fe (100), (110), and (111) surface oxidation processes in a borate buffer solution at pH 8.4 was investigated by *in situ* x-ray reflectivity experiments. Three

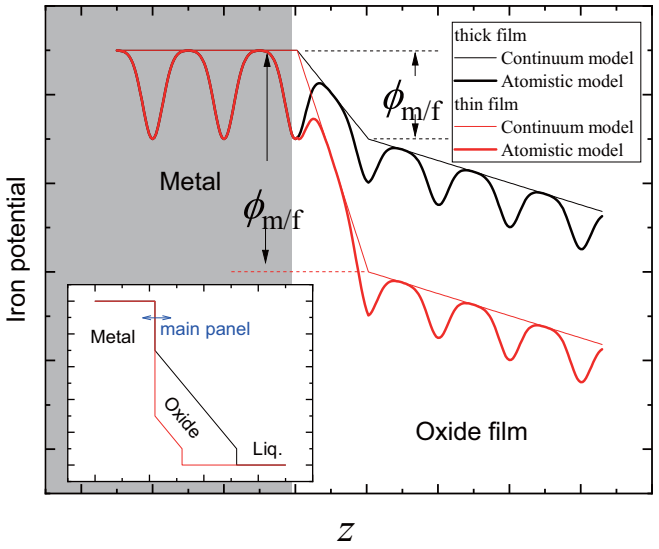

FIG. 7. Schematic of the iron potential profile around the metal-oxide interface. The thin curves show the profiles for the continuum approximation or ordinary PDM, and the thick curves show the profiles for the atomistic model. Black and red profiles show the situations for thick oxide film and thin oxide film cases, respectively. $\phi_{m/f}$ denotes the potential difference between the metal and the oxide regions (see the text). Inset: The potential curve for a wider z range used for ordinary PDM.

distinct stages in the film growth process were observed. In stage I, the film density was less than in the later stages and the suggested structure was a highly defective spinel oxide. The density monotonically increased with time and reached the same value as a later stage at the end of stage I. An atomistic interpretation of this defective growth is discussed. The growth rate followed $dL/dt \propto t^{-1.5}$ during stages Iand II, which is not explained by the well-known growth laws such as the diffusion limited law $dL/dt \propto t^{-1/2}$. During stage II, the deviation of the thickness dependence of the growth rate from that in stage III, $dL/dt \propto \exp(-AL)$, was small, while the qualitative behavior of dL/dt as a function of t was clearly different. Stage IIIpresented a typical behavior following PDM in which the relationships $dL/dt \propto t^{-1}$ and $dL/dt \propto \exp(-AL)$ were expected. Surface orientation influences the growth rate as a function of thickness, which is caused by the lattice mismatch.

ACKNOWLEDGMENTS

The authors thank H. Tajiri for experimental support and K. Nagai for help with the analysis. This work was supported by Grants-in-Aid for Scientific Research (JSPS KAKENHI, Grants No. JP26287080 and No. JP26105008) and the MEXT Elements Strategy Initiative to Form Core Research Center (Grant No. JPMXP0112101001). The synchrotron radiation experiments at SPring-8 were performed with the approval of the Japan Synchrotron Radiation Research Institute (JASRI) (Proposals No. 2017A0908, No. 2017B0908, No. 2018A1135, No. 2018A0908, No. 2018B0938, and No. 2019A0938).

[1] M. M. Lohrengel, Thin anodic oxide layers on aluminium and other valve metals: High field regime, Mater. Sci. Eng. R **11**, 243 (1993).

[2] N. Sato and M. Cohen, The kinetics of anodic oxidation of iron in neutral solution: I. steady growth region, J. Electrochem. Soc. **111**, 512 (1964).

[3] R. V. Moshtev, Steady state film growth on passive iron in neutral solutions, Ber. Bunseng. Physik. Chem. **71**, 1079 (1967).

[4] M. Nagayama and M. Cohen, The anodic oxidation of iron in a neutral solution: I. The nature and composition of the passive film, J. Electrochem. Soc. **109**, 781 (1962).

[5] A. Veluchamy, D. Sherwood, B. Emmanuel, and I. S. Cole, Critical review on the passive film formation and breakdown on iron electrode and the models for the mechanisms underlying passivity, J. Electroanal. Chem. **785**, 196 (2017).

[6] Y. Y. Andreev, Thermodynamic calculation of flade potential of fe, ni, and cr taking into account surface energy, Protect. Metals Phys. Chem. Surf. **45**, 669 (2009).

[7] Y. Y. Andreev and T. V. Bobkov, Chemisorption model of electrochemical passivity of metals and thermodynamic calculation of the flade potential of metals ni and cr taking into account their surface gibbs energy, Protect. Metals Phys. Chem. Surf. **51**, 730 (2015).

[8] N. Cabrera and N. F. Mott, Theory of the oxidation of metals, Rep. Prog. Phys. **12**, 163 (1949).

[9] C. Y. Chao, L. F. Lin, and D. D. Macdonald, A point defect model for anodic passive films: I. film growth kinetics, J. Electrochem. Soc. **128**, 1187 (1981).

[10] D. D. Macdonald and M. Urquidi-Macdonald, Theory of steady-state passive films, J. Electrochem. Soc. **137**, 2395 (1990).

[11] D. D. MacDonald, The history of the point defect model for the passive state: A brief review of film growth aspects, Electrochim. Acta **56**, 1761 (2011).

[12] D. H. Kim, S. S. Kim, H. H. Lee, H. W. Jang, J. W. Kim, M. Tang, K. S. Liang, S. K. Sinha, and D. Y. Noh, Oxidation kinetics in iron and stainless steel: An in situ x-ray reflectivity study, J. Phys. Chem. B **108**, 20213 (2004).

[13] J. Kruger and J. P. Calvert, Ellipsometric-potentiostatic studies of iron passivity: I. anodic film growth in slightly basic solutions, J. Electrochem. Soc. **114**, 43 (1967).

[14] Z. Szklarska-Smialowska and W. Kozlowski, Electrochemical and ellipsometric investigations of passive films formed on iron in borate solutions: I. the kinetics of film growth on iron at constant anodic potentials, J. Electrochem. Soc. **131**, 234 (1984).

[15] K. N. Goswami and R. W. Staehle, Growth kinetics of passive films on Fe, Fe-Ni, Fe-Cr, Fe-Cr-Ni alloys, Electrochim. Acta **16**, 1895 (1971).

[16] C. Lukac, J. B. Lumsden, S. Smialowska, and R. W. Staehle, Effects of temperature on the kinetics of passive film growth on iron, J. Electrochem. Soc. **122**, 1571 (1975).

[17] H. Fujii, Y. Wakabayashi, and T. Doi, Kinetics of iron passivation studied by sub-second resolution realtime x-ray reflectivity technique, J. Electrochem. Soc. **166**, E212 (2019).

[18] T. Doi, T. Kamimura, and M. Sato, Electrochemical phase change of iron rusts by *in-situ* x-ray diffraction technique, Mater. Trans. **53**, 1536 (2012).
[19] T. Ohtsuka and H. Yamada, Effect of ferrous ion in solution on the formation of anodic oxide film on iron, Corr. Sci. **40**, 1131 (1998).
[20] M. Anada, Y. Nakanishi-Ohno, M. Okada, T. Kimura, and Y. Wakabayashi, Bayesian inference of metal oxide ultrathin film structure based on crystal truncation rod measurements, J. Appl. Cryst. **50**, 1611 (2017).
[21] N. Sato, K. Kudo, and T. Noda, The anodic oxide film on iron in neutral solution, Electrochim. Acta **16**, 1909 (1971).
[22] N. Sato and K. Kudo, Ellipsometry of the passivation film on iron in neutral solution, Electrochim. Acta **16**, 447 (1971).
[23] K. Ueda and R. Shimizu, LEED-work function studies on fe (100), Jpn. J. Appl. Phys. **11**, 916 (1972).
[24] H. Kobayashi and S. Kato, Observations on the photoelectric work function and leed pattern from the (111) surface of an iron single crystal, Surf. Sci. **18**, 341 (1969).
[25] A. J. Davenport, L. J. Oblonsky, M. P. Ryan, and M. F. Toney, The structure of the passive film that forms on iron in aqueous environments, J. Electrochem. Soc. **147**, 2162 (2000).
[26] M. Vankeerberghen, 1d steady-state finite-element modeling of a bi-carrier one-layer oxide film, Corrosion Sci. **48**, 3609 (2006).
[27] C. Bataillon, F. Bouchon, C. Chainais-Hillairet, C. Desgranges, E. Hoarau, F. Martin, S. Perrin, M. Tupin, and J. Talandier, Corrosion modeling of iron based alloy in nuclear waste repository, Electrochim. Acta **55**, 4451 (2010).
[28] A. J. Samin and C. D. Taylor, A one-dimensional time-dependent model for studying oxide film growth on metallic surfaces, J. Appl. Phys. **123**, 245303 (2018).
[29] J. Gui and T. M. Devine, In situ vibrational spectra of the passive film on iron in buffered borate solution, Corros. Sci. **32**, 1105 (1991).
[30] V. Schroeder and T. M. Devine, Surface enhanced Raman spectroscopy study of the galvanostatic reduction of the passive film on iron, J. Electrochem. Soc. **146**, 4061 (1999).
[31] S. P. Harrington, F. Wang, and T. M. Devine, The structure and electronic properties of passive and prepassive films of iron in borate buffer, Electrochim. Acta **55**, 4092 (2010).
[32] A. J. Davenport and M. Sansone, High resolution in situ XANES investigation of the nature of the passive film on iron in a pH 8.4 borate buffer, J. Electrochem. Soc. **142**, 725 (1995).
[33] M. P. Ryan, R. C. Newman, and G. E. Thompson, An STM study of the passive film formed on iron in borate buffer solution, J. Electrochem. Soc. **142**, L177 (1995).
[34] M. F. Toney, A. J. Davenport, L. J. Oblonsky, M. P. Ryan, and C. M. Vitus, Atomic Structure of the Passive Oxide Film Formed on Iron, Phys. Rev. Lett. **79**, 4282 (1997).
[35] J.-L. Hazemann, J. F. Bérar, and A. Manceau, Rietveld studies of the aluminium-iron substitution in synthetic goethite, Mater. Sci. For. **79-82**, 821 (1991).
[36] F. J. Ewing, The crystal structure of lepidocrocite, J. Chem. Phys. **3**, 420 (1935).
[37] J. B. Parise, W. G. Marshall, R. I. Smith, H. D. Lutz, and H. Möller, The nuclear and magnetic structure of "white rust"-$Fe(OH_{0.86}D_{0.14})_2$, Am. Mineral. **85**, 189 (2000).
[38] W. D. Birch, A. Pring, A. Reller, and H. W. Schmalle, Bernalite, $Fe(OH)_3$, a new mineral from Broken Hill, New South Wales: Description and structure, Am. Mineral. **78**, 827 (1993).
[39] S. C. Hendy, N. J. Laycock, and M. P. Ryan, Atomistic modeling of cation transport in the passive film on iron and implications for models of growth kinetics, J. Electrochem. Soc. **152**, B271 (2005).